HAL
open science

Kinematical and thermal fields observations associated with the Portevin Le Châtelier effect on an Al-Mg alloy

Hervé Louche, K. Bouabdallah, Pierre Vacher, T. Coudert, P. Balland

To cite this version:

Hervé Louche, K. Bouabdallah, Pierre Vacher, T. Coudert, P. Balland. Kinematical and thermal fields observations associated with the Portevin Le Châtelier effect on an Al-Mg alloy. ASME Applied Mechanics and Materials Conference, Jun 2007, Austin, United States. 10.1007/s11340-008-9125-5 . hal-00343943

HAL Id: hal-00343943

https://hal.science/hal-00343943v1

Submitted on 21 Dec 2018

HAL is a multi-disciplinary open access archive for the deposit and dissemination of scientific research documents, whether they are published or not. The documents may come from teaching and research institutions in France or abroad, or from public or private research centers.

L'archive ouverte pluridisciplinaire **HAL**, est destinée au dépôt et à la diffusion de documents scientifiques de niveau recherche, publiés ou non, émanant des établissements d'enseignement et de recherche français ou étrangers, des laboratoires publics ou privés.

Experimental Mechanics
DOI 10.1007/s11340-008-9125-5

Kinematic Fields and Acoustic Emission Observations Associated with the Portevin Le Châtelier Effect on an Al–Mg Alloy

H. Louche · K. Bouabdallah · P. Vacher · T. Coudert · P. Balland

Received: 4 September 2007 / Accepted: 15 January 2008
© Society for Experimental Mechanics 2008

Abstract This paper presents experimental tensile test results obtained on flat aluminum magnesium alloy samples on a hard machine. The mechanical response, kinematic fields and acoustic emissions were simultaneously obtained in an experimental setup. Propagation instabilities associated with the Portevin–Le-Châtelier effect were observed as localized intense strain increment bands. Depending on the strain rate, A, B or C types were studied on the basis of stress drops, acoustic emission and strain fields. Then the band characteristics (position, orientation, width, thickness reduction, intensity, acoustic emission, principal strain direction) were presented in various strain rate conditions.

Keywords Portevin–Le-Châtelier effect · Strain field measurement · Acoustic emission · Strain localization · Aluminum magnesium alloy

Introduction

The Portevin–Le-Châtelier (PLC) effect is often described as an unstable phenomenon with the localization of plastic flow and serrated yield visible in the load response [1–7]. Metal alloys can be affected by this behavior when they are deformed at suitable temperatures and strain rates. Three generic types of serration are usually identified (A, B and C), depending on the strain rate and temperature range. When the strain rate decreases, one can successively observe A-type bands associated with continuous propagation, B-type bands associated with hopping propagation and C-type bands which are randomly nucleated [8–14].

Many experimental studies, particularly on AlMg alloys, have been carried out. Many of them were focused on different kinds of serration in the load response [3–9, 13]. Others involved a clip-on extensometer, which limited localization detection and analysis [6, 7, 15, 16]. Recent advances in optical methods and image processing have enabled new investigations on the mechanical behavior of materials. Using a multizone laser extensometer [11, 12], estimated local strain in the axial direction, with 20 separate measurement points. With this experimental procedure, they were able to classify the bands in the three conventional types (A, B and C), depending on the strain rates and temperature. An improvement of spatial and temporal resolutions of this one-dimensional technique can be found in [17] with applications to B-type band detection velocity measurement. A laser technique was proposed by [18] to collect bi-dimensional information on PLC bands. Their qualitative observations were used to study the effects of strain, strain rate, sample thickness and ageing on band width, velocity and angle. Using 2D Digital Image Correlation (DIC) software [19], measured strain fields during nucleation of the B-type band. They showed that the band was formed within a few milliseconds. Using a similar technique, Digital Speckle Correlation-DSC [20, 21], measured displacement and strain fields during nucleation and growth of the three types of PLC bands. They showed that the A-type band intermittently propagated with steps smaller than the band width. More recently [22], used DIC to analyze the influence of prestrain at low temperature (223 K) on PLC banding at room temperature. They measured incremental plastic strains within the bands and showed that prestrains of 0.1 or higher changed the nature of the PLC bands.

H. Louche (✉) · K. Bouabdallah · P. Vacher · T. Coudert · P. Balland
SYMME, Polytech'Savoie,
Université de Savoie, BP 80439,
74944 Annecy Le Vieux Cedex, France
e-mail: herve.louche@univ-savoie.fr

In addition to these spatial descriptions, other researchers have worked on the acoustic emission (AE) feature of the PLC effect (see [23–26], for example). AE is a phenomenon linked to elastic waves generated within the material because of sudden localization of the dislocation movement associated with the PLC effect. Recently [27, 28], combined AE and one-dimensional laser extensometry to study Lüders band propagation and the B and C-type bands in the PLC effect on an Al–1.5% Mg alloy deformed at low and moderate strain rates. In this study, they tried to correlate AE and a strain event location.

The objectives of the present study were to obtain experimental results on the spatiotemporal behavior of PLC bands in order to improve material models as presented, for example, in [14]. As a supplement to some preliminary work on the kinematics, thermal and dissipative effects associated with the PLC phenomenon [29, 30], this paper presents quantitative kinematics and AE coupled measurements obtained in tensile tests on an AlMg alloy. The first part of the paper describes the experimental procedure, with a presentation of the tests and techniques used to measure strain fields and AE. Then typical experimental results are presented. The local strain field results are compared to the nominal stress–strain response and to the AE for various band types associated with different imposed strain rates.

Experimental Procedure

Material and Test Features

The flat samples (160×20.4×1 mm) were machined from a commercial Al–3.3% Mg (wt.%) alloy sheet (A5854). Room temperature tensile tests were conducted at different imposed displacement rates, corresponding to four mean nominal strain rates: 10^{-2}, 10^{-3}, 10^{-4} and 10^{-5} s^{-1}. To simplify the notation, these tests will be named 'PLCn', for the test conducted at the imposed strain rates (10^{-n} s^{-1}).

Acoustic Emission Measurement

Three experimental synchronized signals were recorded during the tests: a conventional load displacement response, longitudinal vibrations and strain fields on the surface of the sample. The load and displacement are given by the tensile machine (Instron 5569) and were recorded with the same data acquisition tool (Siglab) as used for the vibration data, at a maximum sampling frequency of 51.2 kHz. The longitudinal vibrations of the sample were recorded to study the typical AE associated with the PLC effect. Vibration data were measured with a high sensitivity piezoelectric accelerometer (Kistler K-shear 5 g, sensitivity=1 V/g) placed in the axial direction on a fixed grip (Fig. 1). A low pass filter included in the Siglab card avoided the risk of aliasing.

Strain Field Measurement

The strain fields were obtained using Digital Image Correlation software (DIC, [31–33]) processing developed in the laboratory [34], which requires random gray levels of the sample surface (Fig. 1). This kind of distribution can be easily obtained by using black and white spray paint. Tests are conducted at ambient lighting with a numerical camera (HAMAMATSU), which records black and white 1,280×1,024 pixel images at 9 Hz maximum. The analysis of the images recorded during the test involved detecting point displacements precisely on the sample surface. The method looks for the most similar pattern between two images, in terms of gray levels, after application of a transformation describing the displacement and deformation of the object. A coefficient of correlation was obtained to quantify the level of resemblance of both sub-images (10×10 pixels) of the pattern in both configurations before and after deformation. This method offers a significant number of measurement points (up to 10,000). For the tests presented in this paper, the number of points in the axial (x) and transverse (y) directions are denoted N_x and N_y. The spatial resolutions, i.e. the distances between two measured points, are the same in the two directions, they are denoted Δx. All strains were calculated using a Green–Lagrange tensor, noted E. This correlation approach calculates the strain field within the 0.01% to 300% range.

The displacement accuracy of the DIC approach is typically about 0.01 pixel for deformations under 5%, but this value depends on many parameters, e.g. image quality, strain gradient and the order of the transformation describing the local deformation. The grey level interpolation chosen in the software was bicubic and the strain fields were computed on the basis of bilinear expression of the displacement distribution in the space. The optimisation method used to find the minimum correlation function was a gradient method. With the above characteristics, and a correlation pattern of 12×12 pixels, errors under 0.01 pixels were obtained in the displacement fields for: (a) rigid body motions imposed on synthetic images, and (b) for homogeneous deformation imposed on synthetic images [35]. The tests: a) were conducted in [35, 36], respectively for imposed displacement amplitudes limited to 0.1 mm and 1 pixel. In [35], a rigid body displacement was imposed along the horizontal x axis (about 100 μm or 4.4 pixels), there was no rotation and of course no deformation. The displacement measured by using digital image correlation was 105.6±0.2 μm and 0.039±0.3 μm, respectively in the x and y directions. The dimension of the grid was 10×10 pixels, the dimension of the pattern used to compare both sub images was 10×10 pixels, the

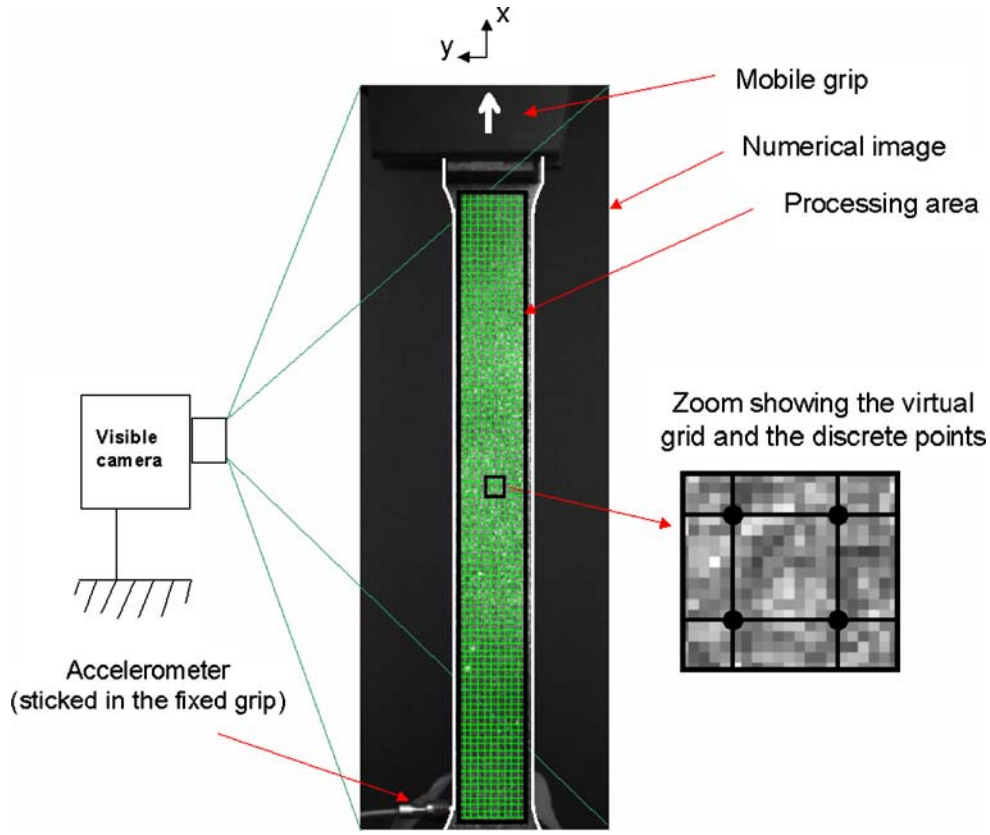

Fig. 1 Experimental setup, showing the grips used for the tensile test, the flat sample, the accelerometer, the digital camera and the discrete virtual grid on which the displacement and strain fields are calculated

displacement field has a bi-linear form and the grey level interpolation was bi-cubic. The mean displacement value was 4.4084 pixels and the standard deviation was σ= 0.00324 pixels. For this analysis, the uncertainties on the displacement field were $\pm 3\sigma \approx \pm 0.01$ pixel. Similar results were obtained in [36].

Furthermore, a recent study [37, 38] conducted by a French research group of 10 laboratories studied the characteristics and performances of seven DIC software packages (Aramis-2D, Correla, Correli, CorrelManuV, KelKins, Vic2D and 7D). In this paper, series of synthetic images with random patterns have been generated. They were submitted to sinusoidal displacements with various frequencies and amplitudes. The RMS error in displacements of the several DIC packages (included the "7D" software used in this work) was less than 0.01 pixels, for pattern size starting from 9 to 31 pixels and strain amplitude from 0.005 to 0.02.

Strain uncertainties are, moreover, a function of the grid dimension (about 0.1% for a square grid with 10×10 pixels and 0.01% for 100×100 pixels). In our experiment, the analysed field was 50×50 mm^2 and the digital camera presented about one million pixels. So the width of one pixel was 0.05 mm. With the DIC approach, it is possible to detect displacements with an accuracy of better than 0.01 pixel, so the accuracy for the displacements was 0.5 μm for the performed tests.

Finally, we assumed that the out-of-plane displacement effects were negligible on the strain field measurements. This assumption was based on the fact that these displacements were supposed small compared to the distance L (about 300 mm) between the camera lens and the sample plane. Both the rigid body motion, when the sample was loaded, and the displacements in the PLC bands were small in the out of plane direction. The latter displacement can be estimated on the basis of the results presented in the last figure of this paper. The maximum displacements in the out of plane direction in the bands were estimated at 0.02 mm. The perturbation of the strain, in the plane, due to this out of plane displacement can be measured on the basis of the relation given in [39]: $\varepsilon = \ln\left(\frac{L}{L-\Delta L}\right)$, where L is the distance between the lens of the camera and the plane of the sample and ΔL is the out of plane displacement. Using L=300 mm and ΔL=0.02 mm, the perturbation in the logarithmic strains was about 6.66×10^{-5} and could be neglected.

Results and Discussion

Global Analysis

Table 1 gives information on strain rates and sample frequencies of the various data acquisitions. For tests carried out at 10^{-2}, 10^{-3} and 10^{-4} s^{-1} (respectively called

Table 1 Description of the tests

Test name	$\dot{\varepsilon} = \frac{V_{\text{cross head}}}{L_0}$ (s^{-1})	Accelerometer sampling frequency (Hz)	Acquired image number	Image sampling frequency (Hz)
PLC2	10^{-2}	2,560	150	4.5
PLC2bis	10^{-2}	5,120	150	9
PLC3	10^{-3}	512	150	0.45
PLC4	10^{-4}	128	150	0.045
PLC5	10^{-5}	512	50	0.111

PLC2, PLC3, PLC4), the whole sample was observed throughout the test. For the test carried out with $\dot{\varepsilon} = 10^{-5}\,s^{-1}$ (PLC5), only a third of the sample surface was analyzed for a short period, corresponding to a reloading of between 13.8% and 14.2% of the total plastic strain. The stress was the nominal stress obtained by the ratio of the load on the initial cross-section.

We observed almost complete overlap of the tensile responses of tests PLC2, PLC3, and PLC4 for respective mean strain rates of 10^{-2} to 10^{-4} s^{-1} [Fig. 2(a)]. It is, however, interesting to note the negative strain rate sensitivity effect, which is well known for the PLC phenomenon and related to the dynamic strain ageing effect [8, 13, 40, 41], i.e. the flow stress decreases when the strain rate increases.

Figure 2(b) and (c) show close-ups of the stress–strain diagram shown in Fig. 2(a), centered around 3.88% and 23.3% of the total strain, respectively. The stress drops were not always regular at the beginning, when the first instabilities appeared. This was the case in high strain rate tests (10^{-3} and 10^{-4} s^{-1}), where irregular stress drops were progressively followed by regular stress drops. This modification in serrations is usually associated with the transition from an A-type band to B or C-type bands [8–11].

For B or C-type bands, each stress drop was associated with band nucleation. For a given test velocity, the number of bands decreased with the strain [42]: for $\dot{\varepsilon} = 10^{-4}\,s^{-1}$, we observed 1.4 bands per second at a strain of 3% and 0.7 band per second at a strain of 20.5%. Moreover, the stress drop amplitude increased with the strain, which is usually linked with the intensity of plastic strains [43].

It was also noted that the slopes during reloading systematically corresponded to the Young modulus observed during the initial elastic loading [approximately

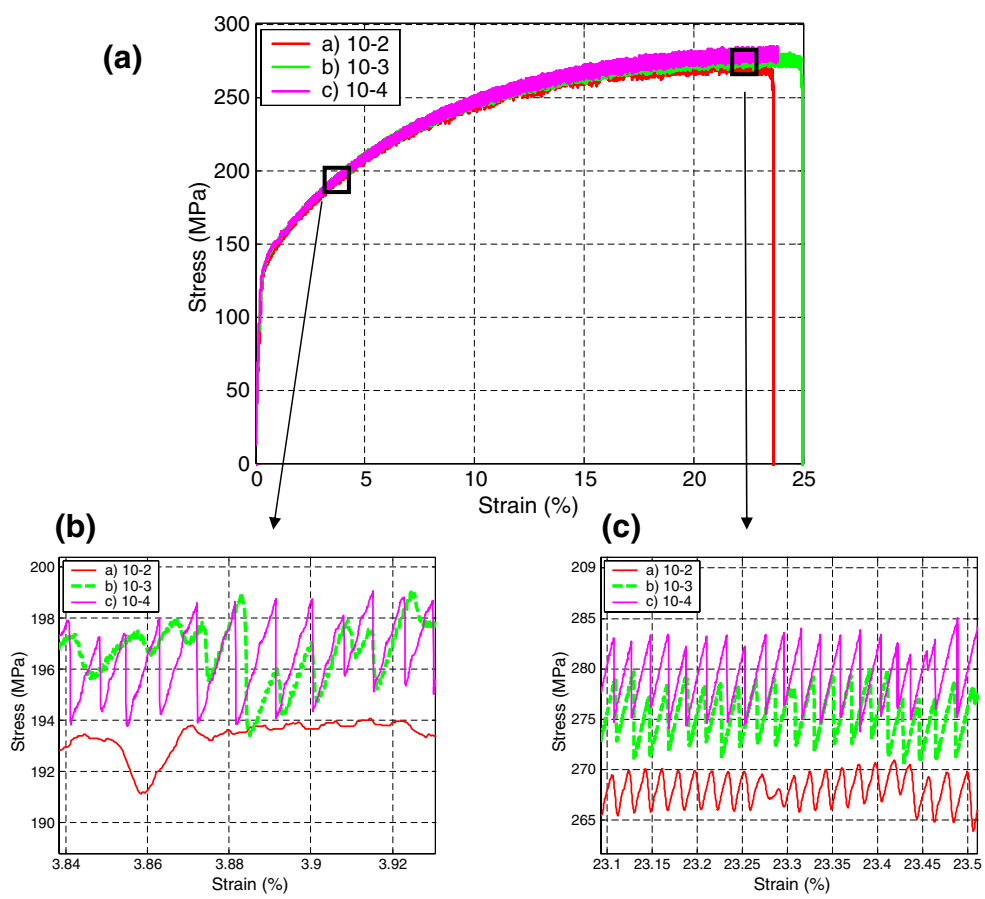

Fig. 2 (**a**) Nominal stress strain responses at different velocities (*a*) 10^{-2} s^{-1} (PLC2), (*b*) 10^{-3} s^{-1} (PLC3), (*c*) 10^{-4} s^{-1} (PLC4); (**b**) and (**c**) close-up of the previous curves, respectively close to 3.88% and 23.3% of the nominal strain, showing regularisation of stress drops for high strains

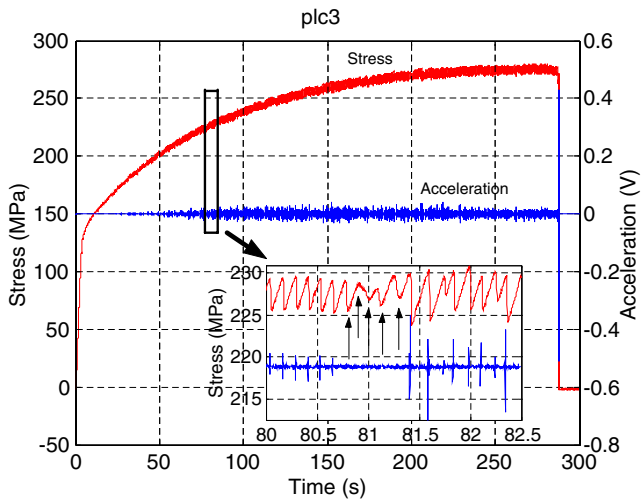

Fig. 3 Test PLC3 (10^{-3} s^{-1}). Temporal variations in the nominal stress and axial acceleration. A close-up of the previous curves shows the relations between some types of stress drops and AE. The *arrows* in the close-up show that some "smooth" stress drops are not systematically correlated with AE events

70,000 MPa; Fig. 2(c)]. This value was measured using DIC software, with a gauge length of 700 pixels.

Analysis at High Strain Rates

Typical results at high strain rates (PLC3=10^{-3} s^{-1} and PLC2=10^{-2} s^{-1}) are presented first. For each test, using a high sensitivity accelerometer, we observed intense vibrations linked to AE that is usually associated with the PLC effect. Generally, a good correlation between the sudden load drops and the AE events was detected (Fig. 3), as also demonstrated in other studies [23–28]. The AE amplitude increased with the strain and depended on the stress drop amplitude, and the sharp drops generally corresponded to high vibration amplitudes. However, no AE was detected during some stress drops (see arrows in the close-up on Fig. 3). This situation happened each time the stress drop rates were less intense. A microscopic origin could explain this behavior. The load drop may have been due to a multislip mechanism of coarse slip bands involved in the band movements, instead of a sudden unpinning of dislocations [24]. These observations contrast with those of [26]. In their work, major AE events appeared in regions where serrations temporarily became irregular. Figure 3 corresponds to a test at 10^{-3} s^{-1}, where the strain fields reveal a B-type band.

The image analysis technique provided a lot of additional information. For the high strain rate (10^{-2} s^{-1}; test PLC2), Fig. 4 shows the strain fields E_{xx} at different loading times. The *xy* plane corresponds to the sample plane, and the axial direction is *x* (see Fig. 1). The strain values are represented in the third axis or with a color scale. For this test, the resolution was N_x=94 and N_y=11 points, and the spatial resolution was Δx=0.174 mm. The gradients in these strain fields revealed the presence of PLC bands, oriented with regards to the loading direction. The band positions and the mean strain amplitudes changed with time. Due to the sample geometry and the type of loading, the localization was developed mainly in the axial direction. An interesting feature is plotted in Fig. 5(a) which presents temporal variations in an axial strain profile $E_{xx}(x, y_0, t)$, where *x* is a current axial position, y_0 is a fixed median transverse position in the sample and *t* is the current time. The nominal stress curve is superimposed in order to correlate serrations with the strain fields. The shape of the gradients observed in this spatiotemporal pattern shows that the strain, for a fixed spatial position, increased stepwise.

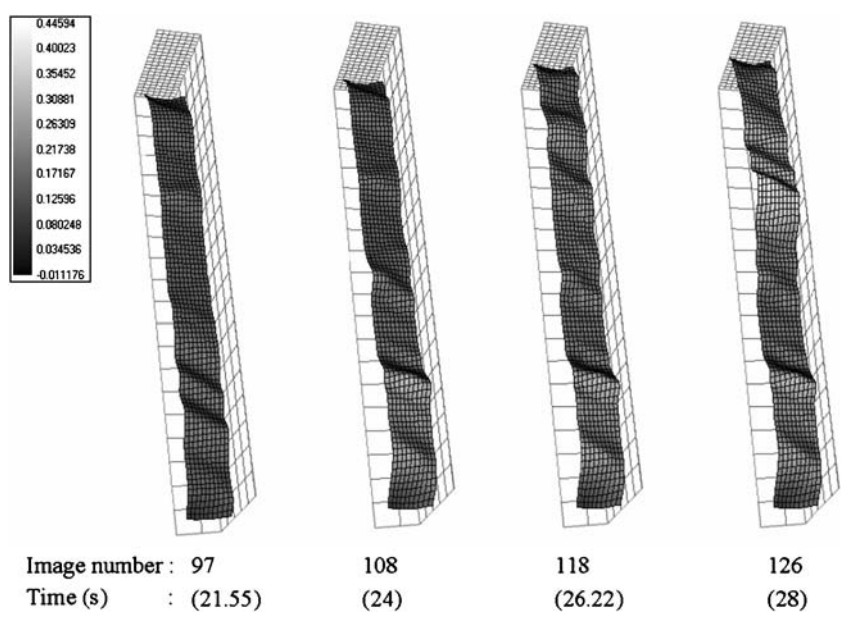

Fig. 4 Test PLC3 (10^{-3} s^{-1}). Green–Lagrange axial strain fields E_{xx} at four times of the loading, showing PLC bands

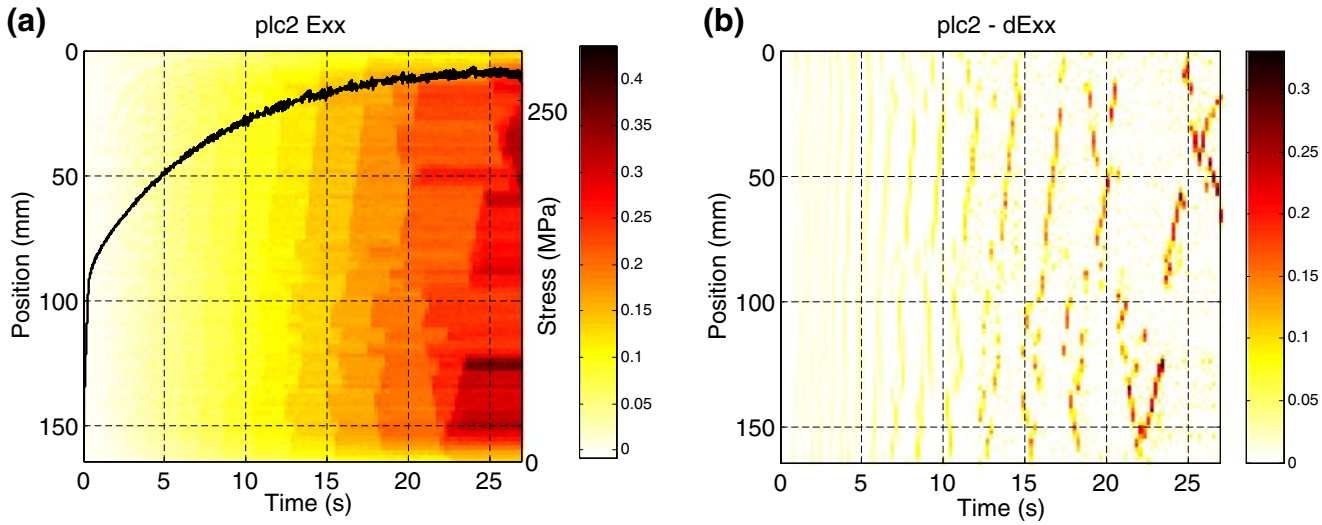

Fig. 5 Test PLC2 (10^{-2} s^{-1}). (**a**) Temporal variations in an axial profile of the Green–Lagrange axial strain, noted $E_{xx}(x, y_0, t)$. The strain intensity is given by the color intensity of the colorbar plotted on the right. The superimposed curve represents the nominal stress. (**b**) Temporal variations in an axial profile of the Green–Lagrange axial strain rate, denoted $dE_{xx}(x, y_0, t)$. This representation enhances the contrast of the previous figure. It shows spatio-temporal characteristics of A-type bands

This situation was associated with a repeated crossing of continuous A-type PLC bands. In order to enhance band detection, we plotted the axial strain rate fields, denoted dE_{xx} [Fig. 5(b)]. These derivative fields were estimated by finite differences in E_{xx} fields in the time direction. This representation enhanced band detection and could show the continuous character of the propagation. At the beginning, only one band was observed at a fixed time. Most of the bands started near the bottom grip and moved towards the opposite grip at constant velocity. Two bands were observed at the end of the loading, just before failure. As previously mentioned [29, 30, 42], the strain rate intensities and period increased with the strain loading. On the other hand, the band velocity decreased with loading because of the high density of forest dislocations which perturbed the propagation of mobile dislocations. Because of the weakness of the spatial and temporal resolutions, the strain rates in the bands were underestimated. For high strains, the strain rate in the bands exceeded the imposed strain rate (10^{-2} s^{-1}) by more than 30-fold [Fig. 5(b)].

Strain fields, AE and nominal stress were subsequently studied simultaneously in a second test (called PLC2bis), conducted on another sample, at the same velocity (10^{-2} s^{-1}) as PLC2. A reduced area of the sample and a reduced loading period (nominal strain [0.17; 0.27]) were monitored in order to increase the spatiotemporal resolution. As in the previous results, the kinematic fields are presented in terms of spatiotemporal variations, while superimposing the nominal stress and AE pattern (Fig. 6). Multiple PLC bands can be seen in this image. High serration is visible in the stress curve, along with AE activity. Figure 7(a), which shows time-course variations in an axial strain rate profile, highlights PLC band propagation. Only one band could be observed at a fixed time, and the band propagated towards the top or bottom grip. It should be noted that some strain rate bands cannot be observed here because they occur outside of the reduced observation area, e.g. in the interval [4.5, 5 s] or after 7 s. The close-up (around time 4 s) presented in Fig. 7(b) shows that there were substantial stress drops and AE activity during band propagation. The stress and AE signals were perfectly synchronized because they were recorded with the same DSP record card. The visible images used to compute the strain fields were taken with

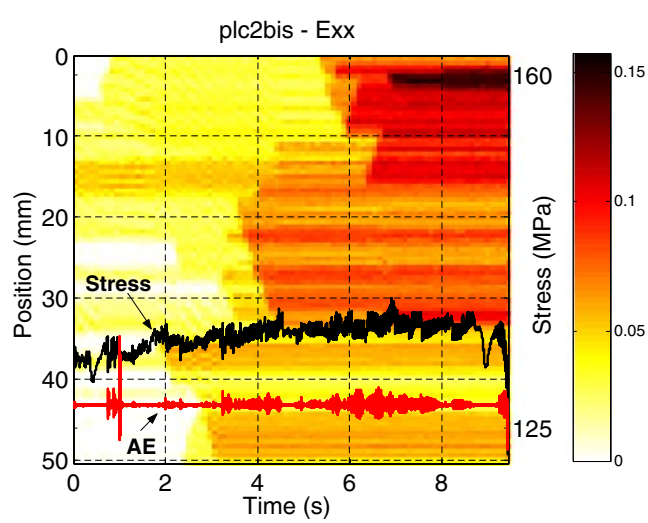

Fig. 6 Test PLC2bis (10^{-2} s^{-1}). Temporal variations in an axial profile of the Green–Lagrange axial strain, denoted $E_{xx}(x, y_0, t)$. The superimposed curves represent temporal variations in the nominal stress and AE

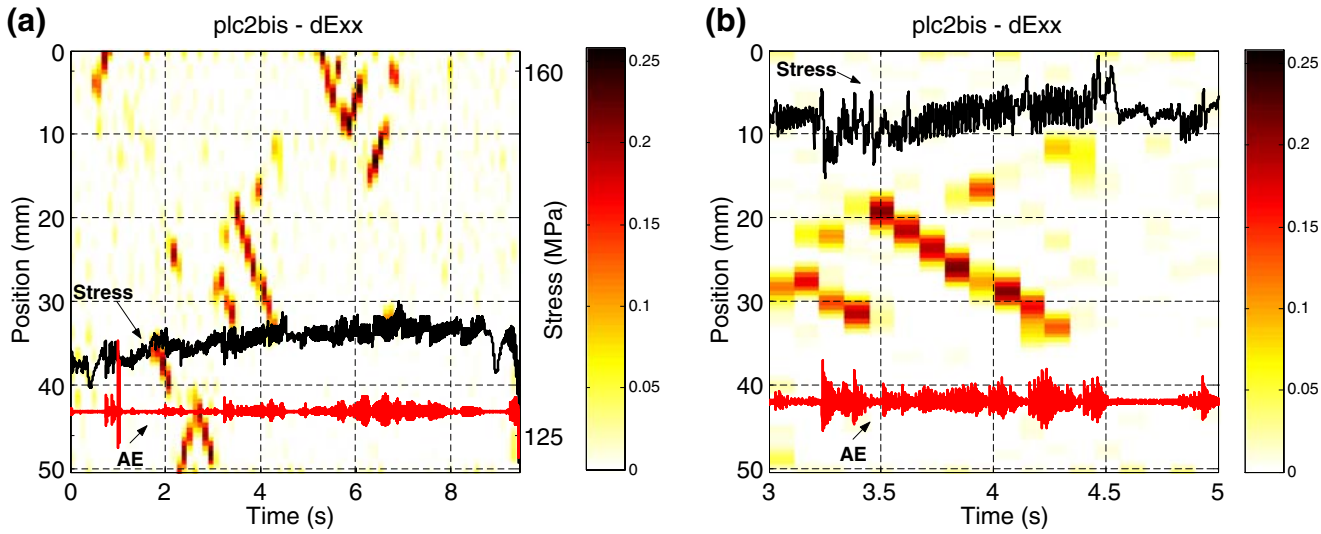

Fig. 7 Test PLC2bis (10^{-2} s^{-1}). (**a**) Temporal variations in an axial profile of the Green–Lagrange axial strain rate, denoted $dE_{xx}(x, y_0, t)$. This representation enhances the contrast. The superimposed curves represent temporal variations in the nominal stress and AE. (**b**) Close-up of the previous figure around time 4 s. It reveals multiple stress drops and AE events during the "apparent" regularity of the propagation of a PLC band

another time base, at a very low frequency (9 Hz) compared with the 5,120 Hz frequency used for the two other signals. So the accuracy of the time synchronization was about 1/9 s, i.e. the period of the images. The multiple stress drops and AE activity during band propagation indicated that the PLC phenomenon seemed discontinuous, as is the case for B-type bands. Here, the spatiotemporal variations in strain (Fig. 6) or in the strain rate [Fig. 7(a) and (b)], showing smooth propagation, is consistent with A-type bands. However, the stress drops and high AE activity are inconsistent with A-type bands. In their recent work [28], noted that for pure A-type bands, AE was intense only during band nucleation, i.e. AE decreased when the bands propagate. The sampling frequency of the camera used in our work (maximum 9 Hz) seemed insufficient to distinguish A-type from B-type bands in the kinematic fields. Complementary experiments, with a high speed camera should now be carried out. Such experiments could show, as recently noted by Xiang et al. [20, 21], that the type A PLC band, traditionally considered as a continuous propagation deformation band, could consist of numbers of forward-propagating, intermittent avalanche-like deformation bands.

Analysis of the Tests at Low Strain Rates

In this part, only a typical result at low strain rate is presented: test PLC5, at 10^{-5} s^{-1}. Using an imposed velocity of 0.1 mm min^{-1}, the test duration was very high (about 6 h), so a reduced observation period of 512 s was chosen. It corresponds to the following nominal strain

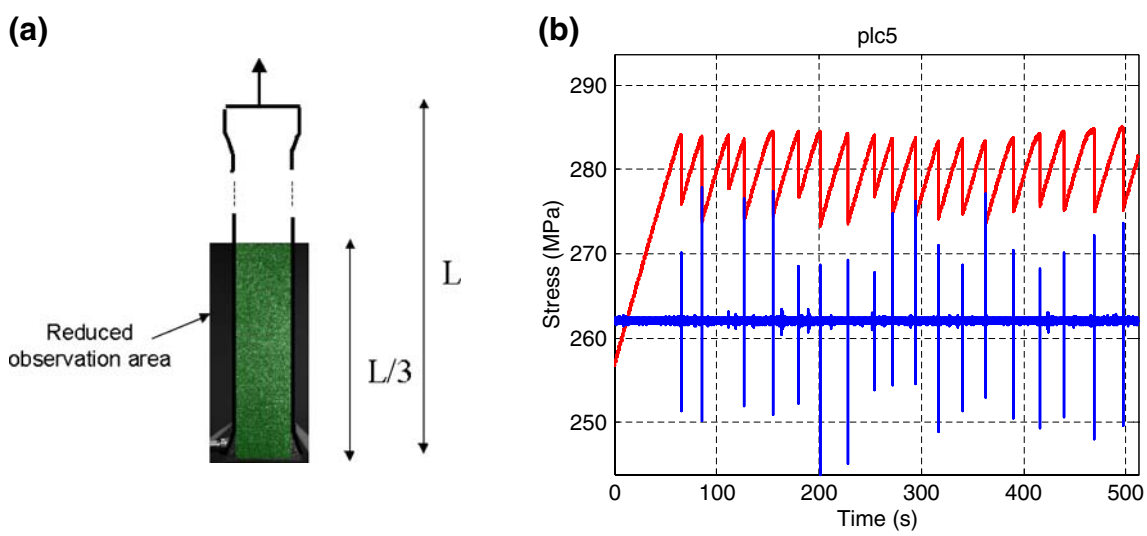

Fig. 8 Test PLC5 (10^{-5} s^{-1}). (**a**) Sketch of the reduced observation area: a third of the sample length. (**b**) Temporal variations in the nominal stress (*above*) and AE (*below*)

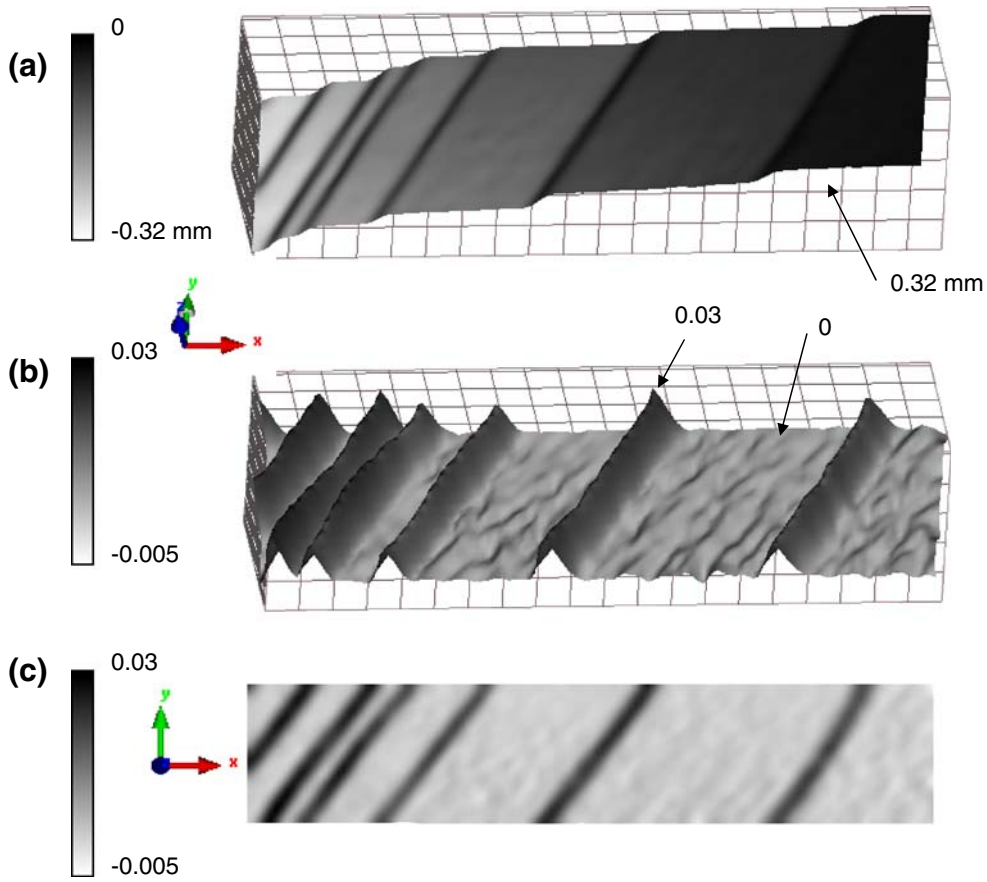

Fig. 9 Test PLC5 (10^{-5} s^{-1}). (**a**) Axial displacement field (in mm), measured at the end of the test (t=450 s) on the sample surface, showing steps corresponding to the contribution of each C-type PLC band. (**b**) Green–Lagrange axial strain field calculated at the same time, showing 6 C-type bands. (**c**) Top view of the previous axial strain field E_{xx}

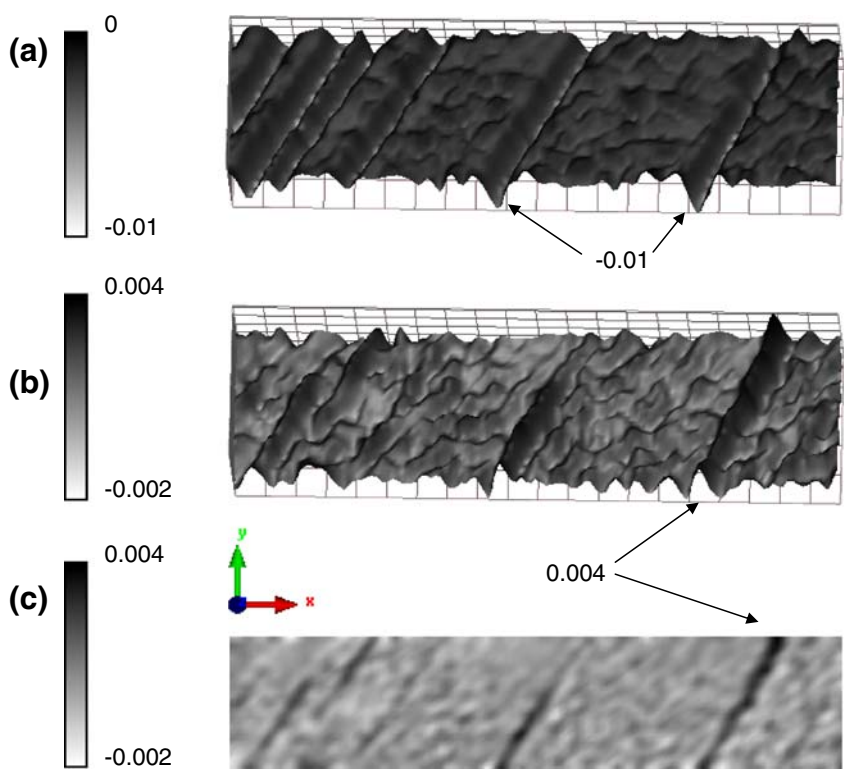

Fig. 10 Test PLC5 (10^{-5} s^{-1}). (**a**) Green–Lagrange transverse Eyy strain field, calculated at the end of the test (t=450 s) on the sample surface, showing 6 C-type bands. (**b**) Green–Lagrange shear strain field E_{xy} calculated at the same time. (**c**) Top view of the previous figure showing low shear strains in some bands

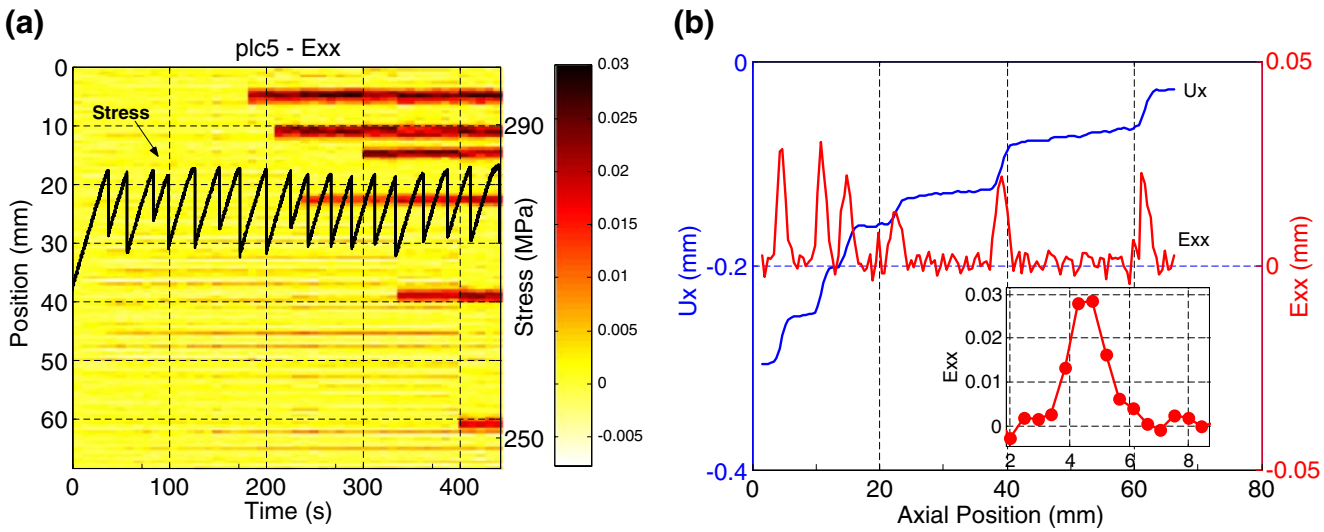

Fig. 11 Test PLC5 (10^{-5} s^{-1}). (**a**) Temporal variations in an axial profile of the Green–Lagrange axial strain, denoted $E_{xx}(x, y_0, t)$. It shows six bands appearing respectively around the positions x=6, 11, 23, 14, 39, 61 mm at the successive times t=176, 209, 235, 296, 328, 396 s. The superimposed curve represents the nominal stress. (**b**) Axial profile of the axial displacement U_x and the Green–Lagrange axial strain E_{xx}, respectively measured and calculated at the end of the test (t=450 s). The close-up around a strain band shows the measured points

interval [13.85%; 14.2%]. Moreover, in order to increase the spatial resolution, the observed images corresponded to approximately a third of the sample length [Fig. 8(a)]. In this case, the spatial resolution was 0.056 mm/pixel instead of 0.174 mm/pixel in the previous observations. At this very low imposed strain rate, high serrations were observed in the load or nominal stress curve [Fig. 8(b)]. Such drops, ranging from 5 to 10 MPa, are compatible with B or C-type bands. Simultaneous AE was measured during loading. The results showed major AE events only at the beginning of

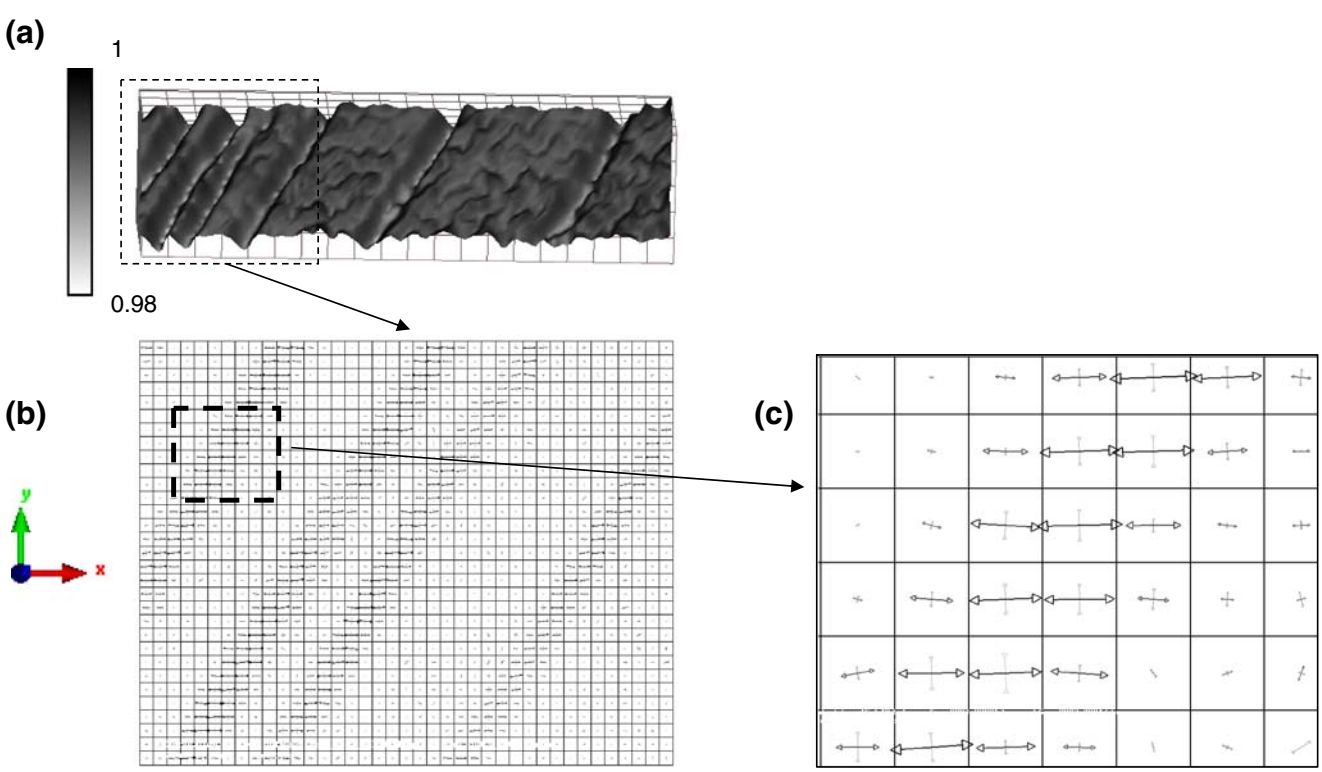

Fig. 12 Test PLC5 (10^{-5} s^{-1}). (**a**) Thickness variation field (in mm), calculated at the end of the test (t=450 s), on the sample surface. (**b**) Principal strain field (in mm), calculated at the end of the test (t=450 s), on the sample surface. (**c**) Close-up of the previous principal strain field. It shows that the principal directions, in the bands, are equal to the axial loading direction (x axis)

the stress drop [Fig. 8(b)], which is associated with the sudden nucleation of a B or C-type band ([28]). AE increased as the stress drops increased.

Figure 9(a) shows, for the PLC5 test, the displacement fields U_x (in mm) in the axial direction observed on the sample surface between the initial (strain: 13.85%) and final images (strain=14.2%). Each step corresponds to the presence of a PLC band. This figure indicates, after converting from the pixel scale to the metric scale, that each band contributed to an elongation of the sample of approximately 0.32 mm. The positions of these bands in the sample, the width and strain distributions in each band are clearly observed in Fig. 9(b) and (c), which presents the axial strain field E_{xx}. Six PLC bands were observed in the processing area during the 512 s of the test. The axial strain intensity in the bands was about 0.03. Transverse strains [Fig. 10(a)] had an amplitude about −0.01 in the band. The shearing strains [Fig. 10(b) and (c)] were very weak, in the (x, y) coordinate system. In some bands, the shear strain values were nonexistent or too low to be detected. Significant shear values were measured only in the two last right bands, and the maximum shear strains were about 0.004 [Fig. 10(c)], which is about a tenth of the axial strains in the same bands. The band angles with respect to the tensile direction was estimated [Fig. 9(c)] at 57±1°, using the mean direction of the bands shape in this figure. A discussion on this value, which is compatible with those reported in the literature, can be found in [30].

In order to detect the band type, a spatiotemporal representation is proposed in Fig. 11(a). It shows time-course variations in an axial strain profile. The stress drop pattern is superimposed. The bands were detected just after the stress drop. The first band detected in the observed area was associated with the seventh stress drop. The sampling frequency (0.111 Hz) was not sufficient to detect the band nucleation right at the beginning of each drop. The spatial positions of the bands were discontinuous and randomly located. This distribution clearly revealed that these were C-type bands.

The shape characteristics of the bands, like the width and amplitude, were difficult to measure because they were strongly dependent on the spatial frequencies of the image acquisition and the image processing. To obtain an accurate approximation, we have to check that the band shape is formed by a sufficient number of points. Figure 11(b) presents an axial profile of the displacement $U_x(x, y_0, t)$ and strain $E_{xx}(x, y_0, t)$ for a fixed transverse position y_0 and a fixed time t=450 s, corresponding to the end of the PLC5 test observation period. The characteristics (position, width, intensity) are clearly presented. The resolution of the image correlation technique is given with the position of the discrete calculated points. The bands were described by only three or four points, which is not sufficient to quantify the width and intensity. However, with these observations, it can be assumed that the real band width was less than the 2.3 mm value estimated here. This also suggests that the strain intensity in the band was higher than the measured value (about 0.03). Based on the volume conservation hypothesis, it is possible to estimate the thickness variation [Fig. 12(a)]. In the band, the lowest thickness reduction bound was 2%. The image correlation software also gives the principal directions and strains on the sample surface plane [Fig. 12(b) and (c)]. This representation shows that, in the bands, the principal strain directions were equal to the axial loading directions, showing that the shear strains were very weak. Unfortunately, the spatial resolution of the images did not allow us to study the principal strain directions in the vicinity of the interface between the band and the bulk. Further experiments with higher spatial resolution would need to be carried out.

Conclusions

Original tensile test experiments, associating measurements of kinematic fields and vibrations with traditional tensile test responses, enabled us to highlight the strongly heterogeneous spatiotemporal character of the PLC phenomenon. From these investigations, we noted various band characteristics like their shapes, distribution and frequency. At high strain rates, A-type bands were observed at the beginning of the loading. When the strain increased, continuous propagation bands (A-type distribution) were observed, but the load drops and multiple AE events suggested B-type bands. Additional experiments with a high-speed camera have to be conducted to distinguish A-type from B-type bands. At low strain rates, C-type bands were clearly detected and linked to the stress drops and AE events. Important band characteristics were measured, such as displacement, strains and thickness variations in the bands. Finally, the principal directions in the bands seemed to coincide with the loading direction showing that the shear strains were very weak. Further experiments with higher spatial resolution would need to be carried out in order to study the transition zone between the band and the bulk.

References

1. Portevin A, Le Châtelier F (1923) Sur un phénomène observé lors de l'essai de traction d'alliages en cours de transformation. C R Acad Sci Paris 176:507–510.
2. Cottrell AH (1953) Dislocations and plastic flow in crystals. Clarendon, Oxford.
3. Hall EO (1970) Yield point phenomena in metals and alloys. Macmillan, London.

4. Chihab K, Estrin Y, Kubin LP, Vergnol J (1987) Kinetics of the Portevin–Le Châtelier in an Al-5atMg alloy. Scr Metall 21:203–208.
5. Kubin LP, Fressengeas C, Ananthakrishna G (2002) Collective behaviour of dislocations in plasticity. In: Nabarro FRN, Duesbery MS (eds) Dislocations in solids. Elsevier, Amsterdam, 11:pp 101–192.
6. McCormick PG, Venkadesan S, Ling CP (1993) Propagative instabilities: an experimental view. Scr Metall Mater 29:1159–1164.
7. Wack B, Tourabi A (1995) A new method to quantify the Portevin–Le Chatelier instabilities: application to aluminium–lithium alloys. Mater Sci Eng A 196:79–87.
8. Chihab K, Ait-Amokhtar H, Bouabdellah K (2002) Serrated yielding due to Portevin–Le Châtelier effect in commercial Al–Mg alloys. Ann Chim 27:69–75.
9. Bharathi MS, Lebyodkin M, Ananthakrishna G, Fressengeas C, Kubin LP (2001) Multifractal burst in the spatiotemporal dynamics of jerky flow. Phys Rev Lett 8716:165508.
10. Bharathi MS, Rajesh S, Ananthakrishna G (2003) A dynamical model for the Portevin–Le Chatelier bands. Scr Metall 48:1355–1260.
11. Ziegenbein A, Hähner P, Neuhäuser H (2000) Correlation of temporal instabilities and spatial localization during Portevin–LeChatelier deformation of Cu–10 at.% Al and Cu–15 at.% Al. Comput Mater Sci 19:27–34.
12. Ziegenbein A, Hähner P, Neuhäuser H (2001) Propagating Portevin–LeChatelier deformation bands in Cu–15 at.% Al polycrystals: experiments and theoretical description. Mater Sci Eng A 309–310:336–339.
13. Lebyodkin M, Dunin-Barkowskii L, Brechet Y, Estrin Y, Kubin L (2000) Spatio-temporal dynamics of the Portevin–Le Chatelier effect: experiment and modelling. Acta Mater 48:2529–2541.
14. Kok S, Beaudoin AJ, Tortelli A, Lebyodkin M (2002) A finite element model for the Portevin–Le Chatelier effect based on polycrystal plasticity. Model Simul Mater Sci Eng 10:745–763.
15. Wijler A, Van den Beukel A (1970) Mobile dislocation density during inhomogeneous deformation in Au(14at%Cu). Scr Metall 4, 9:705–708.
16. Schade J, Van Westrum A, Wijler A (1973) Determination of the characteristics of Portevin_Le-Châtelier bands in Au (14. at %Cu). Acta Metall 21:1079–1086.
17. Casarotto L, Tutsch R, Ritter R, Dierke H, Klose F, Neuhaüser H (2005) Investigation of PLC bands with optical techniques. Comput Mater Sci 32:316–322.
18. Shabadi C, Kumar S, Roven HJ, Dwarakadasa ES (2004) Characterisation of PLC band parameters using laser speckle technique. Mater Sci Eng A 364:140–150.
19. Tong W, Tao H, Zhang N, Hector LG (2005) Time-resolved strain mapping measurements of individual Portevin–Le Chatelier deformation bands. Scr Mater 53:87–92.
20. Zhang QC, Jiang Z, Jiang H, Chen Z, Wu XP (2005) On the propagation and pulsation of Portevin–Le Chatelier deformation bands: An experimental study with digital speckle pattern metrology. Int J Plast 21:2150–2173.
21. Xiang GF, Zhang QC, Liu HW, Wu XP, Ju XY (2007) Time-resolved deformation measurements of the Portevin–Le Chatelier bands. Scr Mater 56:721–724.
22. Halim H, Wilkinson DS, Niewczas M (2007) The Portevin–Le Chatelier (PLC) effect and shear band formation in an AA5754 alloy. Acta Mater 55:4151–4160.
23. Pascual R (1974) Acoustic emission and dislocation multiplication during serrated flow of an aluminum alloy. Scr Metall 8:1461–1466.
24. Caceres CH, Rodriguez AH (1987) Acoustic emission and deformation bands in Al–2.5% Mg Cu–30% Zn. Acta Metall 35:2851–2864.
25. Chmelík F, Trojanová Z, Převorovský Z, Lukáč P (1993) The Portevin–Le Châtelier Effect in Al–2.92%Mg–0.38%Mn alloy and linear location of acoustic emission. Mater Sci Eng A 164:260–265.
26. Reed JM, Walter ME (2003) Observations of serration characteristics and acoustic emission during serrated flow of an Al–Mg alloy. Mater Sci Eng A 359:1–10.
27. Chmelík F, Ziegenbein A, Neuhäuser H, Lukác P (2002) Investigating the Portevin–Le Châtelier effect by the acoustic emission and laser extensometry techniques. Mater Sci Eng A 324:200–207.
28. Chmelik F, Klose FB, Dierke H, Šachl J, Neuhäuser H, Lukáč P (2007) Investigating the Portevin–Le Châtelier effect in strain rate and stress rate controlled tests by the acoustic emission and laser extensometry techniques. Mat Sci Eng A 462:53–60.
29. Ait-Amokhtar H, Vacher P, Boudrahem S (2006) Kinematics fields and spatial activity of Portevin–Le Chatelier bands using the digital image correlation method. Acta Mater 54:4365–4371.
30. Louche H, Vacher P, Arrieux R (2005) Thermal observations associated with the Portevin–Le Châtelier effect in an Al–Mg alloy. Mater Sci Eng A 404:188–196.
31. Peters WH, Ranson WF (1981) Digital image techniques in experimental stress analysis. Opt Eng 21:427–441.
32. Sutton MA, Wolters WJ, Peters WH, Ranson WF, McNeill SR (1983) Determination of displacements using an improved digital correlation method. Image Vis Comput 1:133–139.
33. Chu TC, Ranson WF, Sutton MA, Peters WH (1985) Applications of digital-image-correlation techniques to experimental mechanics. Exp Mech 25:232–244.
34. Vacher P, Dumoulin S, Morestin F,Mguil-Touchal S (1999) Bidimensional deformation measurement using digital images. Proc Inst Mech Engrs 213:811–817.
35. Coudert T (2005) Reconstruction tridimensionnelle du volume intérieur d'une chaussure, évaluation du chaussant. Ph.D. thesis, Université de Savoie, Annecy, France.
36. Dumont F (2003) Contribution à l'expérimentation et à la modélisation de renforts composites tissés. Ph.D. thesis, Université Paris 6, Orléans, France.
37. Orteu JJ (2007) Digital image error correlation (DIC) assessment. SEM Annual Conference, Springfield, MA, USA, June 4–6.
38. Bornert M, Brémand F, Doumalin P, Dupré JC, Fazzini M, Grédiac M, Hild F, Mistou S, Molimard J, Orteu JJ, Robert R, Surrel Y, Vacher P, Wattrisse B (2008) Assessment of digital image correlation software packages. Exp Mech (in press).
39. Gaudin V (2007) Contribution à l'étude de micromuscles artificiels activables par pression osmotique et implantables en milieu biologique. Ph.D. thesis, Université Joseph Fourier, Grenoble, France.
40. Kubin LP, Estrin Y (1985) The Portevin Le Chatelier effect in deformation with constant stress rate. Acta Metall 33:397–407.
41. Balik J (2001) The onset of Portevin–Le-Chatelier instabilities in tensile testing. Mater Sci Eng A 316:102–108.
42. D'Anna G, Nori F (2001) Critical dynamics of burst instabilities in the Portevin–Le Châtelier effect. Phys Rev Lett 85: 4096–4099.
43. Bouabdallah K (2006) Caractérisation de l'effet Portevin–Le Châtelier dans les alliages aluminium magnésium—Apport des techniques d'analyse d'images. Ph.D. thesis, Université de Savoie, France.